RSC Advances

PAPER

View Article Online
View Journal | View Issue

Cite this: *RSC Adv.*, 2017, **7**, 27170

A general seed-mediated approach to the synthesis of AgM (M = Au, Pt, and Pd) core–shell nanoplates and their SERS properties†

Siva Kumar-Krishnan,*[a] M. Estevez-González,[a] Ramiro Pérez,[a] Rodrigo Esparza*[a] and M. Meyyappan[b]

Ag-based bimetallic core–shell nanoplates have received much attention in catalysis, surface-enhanced Raman scattering (SERS), and sensing applications. However, control over the synthesis of core–shell nanostructures still remains a challenge. Herein, we present a facile, seed-mediated synthesis of bimetallic or multimetallic AgM (M = Au, Pt, and Pd) core–shell nanoplates using pre-synthesized triangular Ag nanoplates as seeds in the presence of ascorbic acid, NaOH, and poly(vinylpyrrolidone) at room-temperature. Higher pH was found to be crucial in effectively controlling the galvanic reaction that resulted in a uniform deposition of the shell on the Ag nanoplate seeds. In contrast, synthesizing in a lower pH condition led to the removal of the Ag core *via* galvanic reaction generating triangular hollow nanoframes comprising of bimetallic AgM (M = Au, Pt, Pd) with well-defined interior gaps. The resultant nanostructures were studied for the SERS performance in the solution-phase using an excitation wavelength of 785 nm. Owing to the tunable plasmonic peaks close to near infrared region of the Ag@Au core–shell nanoplates, greatly enhanced SERS signal was obtained compared to the original Ag nanoplates, Ag@Pt, Ag@Pd, and Ag@PtPd nanostructures. Our approach demonstrates control over the galvanic exchange reaction and thereby makes it possible to synthesize intricate architectures on the nanoscale, opening up promising opportunities for rational designing of multifunctional nanostructures for plasmonics and sensing applications.

Received 17th April 2017
Accepted 17th May 2017

DOI: 10.1039/c7ra04301e

rsc.li/rsc-advances

Introduction

Metal nanocrystals (NCs) with controlled size and shape have emerged as an important class of functional nanomaterials for various applications such as catalysis,[1,2] plasmonics,[3] surface enhanced Raman scattering (SERS),[4] biosensing,[5] and biomedicine.[6] In particular, Ag nanoplates can produce intense electromagnetic field enhancements because of their localized surface plasmon resonance (LSPR) properties.[7] Specifically, coupling of these LSPR with the molecular vibrations enables improvement of the sensitivity of the SERS signal.[8–11] However, the stability in ambient condition and easy oxidation toward many chemical reactions often limit their use in practical applications.[7] Substantial research efforts have been directed toward the rational design of bimetallic NCs made of Ag, Au, Pt, and Pd in a core–shell fashion due to their significantly enhanced catalytic activity and SERS properties.[12–16] For example, previous studies have reported that the triangular Ag@Au nanoplates exhibit considerably enhanced SERS activity compared to the original Ag nanoplates because of the hot spots formed at their sharpened edges and nanogaps between Ag and Au.[17,18] Moreover, a combination of Pd and Pt with plasmonic Ag nanocrystals has been shown as a promising approach for efficient *in situ* SERS-based monitoring of catalytic reactions.[14]

To date, several preparation methods such as plasmon-driven synthesis,[19] non-epitaxial growth,[20] epitaxial growth,[21] and halide mediated hydrothermal synthesis[22] have been exploited for the synthesis of core–shell nanostructures. Although some of these methods are remarkable to create monodisperse core–shell nanostructures, it is still a challenge to generate well-defined core–shell NPs with spatially controlled distribution and symmetry. Recently, the seed-mediated solution-phase technique has emerged as a powerful and versatile route for preparing bimetallic or multimetallic core–shell nanocrystals.[23–26] In general, the challenge arises mainly because of the inherent galvanic replacement reaction between the Ag seeds and M-precursors, usually leading to the formation of hallow nanostructures or different NP shapes.[27,28] Numerous groups have extensively investigated the conformal deposition

[a]*Centro de Física Aplicada y Tecnología Avanzada, Universidad Nacional Autónoma de México, Boulevard Juriquilla 3001, Santiago de Querétaro, Qro., 76230, Mexico. E-mail: skumar@fata.unam.mx; resparza@fata.unam.mx*

[b]*Center for Nanotechnology, NASA Ames Research Center, Moffett Field, Mountain View, California 94035, USA*

† Electronic supplementary information (ESI) available: TEM images, UV-vis, XRD analysis, EDX-mapping of trimetallic hallow Ag@PtPd NPs. See DOI: 10.1039/c7ra04301e

of Au/Pd/Pt as a shell on Ag nanocrystals by overcoming the galvanic replacement reaction.[15,16,29] Yin *et al.* described the controlled etching-free epitaxial deposition of Au on Ag nanoplates by reducing the reduction potential of Au^{3+} with iodide (I^-) ions.[17] Qin and co-workers[14,30] and Zhang *et al.*[31] demonstrated, through conformal deposition, Ag@Au nanocubes and Ag@Au concave cuboctahedra core–shell nanocrystals with few atomic layers of Au-shells. Recently, Xia[32] group demonstrated the conformal deposition of Au shell on Ag nanowires to achieve uniform Ag@Au core–shell nanowires under alkaline conditions. Furthermore, the deposition of Au, Pt, and Pd on the surface of the Ag seeds typically adopts a diffusion-mediated island growth mode due to the thermodynamic constraints arising from the high surface energy, which leads to different nanocrystal shapes.[33] To the best of our knowledge, the galvanic replacement-free pH-dependent conformal deposition of Au, Pt and Pd to obtain bimetallic and trimetallic core–shell nanoplates and their optical properties has not been reported previously.

Herein, we describe a simple and general strategy based on galvanic replacement-free deposition approach to prepare bimetallic AgM (Au, Pd, and Pt) and multicomponent system such as Ag@PtPd core–shell nanostructures in a well-controlled fashion at room temperature. The unique feature of our approach is the rapid reduction of metal precursors at higher pH using ascorbic acid (AA), allowing control of the galvanic replacement reaction and consequently, the uniform deposition of metal precursor onto the triangular Ag nanoplate template. Moreover, manipulating the reaction conditions (*e.g.* lowering the pH) enables preparation of bimetallic and multimetallic hollow nanoframes with well-defined interior gaps. Finally, we investigated the SERS properties, which showed remarkably enhanced SERS activity for the Ag@Au nanoplates compared to the Ag@Pt, Ag@Pd and Ag@PdPt core–shell nanoplates.

Experimental

Materials

Silver nitrate ($AgNO_3$, 99%), gold(III) chloride tetrahydrate ($HAuCl_4$, $3H_2O$, 99.9%), palladium(II) chloride ($PdCl_2$, 99.9%), potassium tetrachloroplatinate(II) (K_2PtCl_4, 99.98%), L-ascorbic acid ($C_6H_8O_6$, ≥99%), poly-(vinylpyrrolidone) PVP with an average molecular weight of 55 000, cetyltrimethylammonium bromide (CTAB, 98%) aqueous hydrochloric acid (HCl), sodium hydroxide (NaOH, 98%), trisodium citrate (99%), sodium borohydrate ($NaBH_4$), hydrogen peroxide (H_2O_2, 30 wt% in H_2O), and crystal violet (≥90%) were obtained from Sigma-Aldrich. All regents were used as received and all glassware were cleaned with deionized water (DI) before using in experiments.

Preparation of triangular Ag nanoplate seeds

The triangular Ag nanoplates with an average edge length of *ca.* 20–30 nm were synthesized according to a previously reported method with minor modifications.[34] In a typical synthesis, 0.4 ml of silver nitrate ($AgNO_3$) solution (0.01 M), 0.6 ml of trisodium citrate (0.1 M) were mixed, and the total volume of the reaction solution was fixed at 40 ml by adding deionized (DI) water. The solution mixture was magnetically stirred vigorously at room temperature and 0.4 ml of sodium borohydrate ($NaBH_4$, 100 mM) was rapidly injected into the reaction mixture to initiate the reduction, followed by the addition of 100 μl of hydrogen peroxide (H_2O_2, 30 wt%). After addition of H_2O_2, a sequential change in color was observed in the following manner, light-yellow, yellow, red, green, and finally blue within 3 min of reaction, suggesting the formation of triangle Ag nanoplates. The final products was collected by centrifugation at 12 000 rpm for about 30 min, washed three times using DI water and re-dispersed in DI water for further synthesis work.

Preparation of AgM (M = Au, Pt and Pd) core–shell nanoplates

In a typical synthesis procedure, 2 ml of the suspension of triangular Ag nanoplates seeds (1 mg ml^{-1}), 100 mg of AA, 66.6 mg of PVP, 13 ml DI water were mixed in a 20 ml glass vial. The pH was adjusted to 11 by the addition of 0.5 ml of aqueous NaOH solution (0.2 M) under magnetic stirring at room-temperature. The deposition of Au-shells was initiated by injection of aqueous $HAuCl_4$ (0.1 M, 100 μl) at a relatively slow rate (10 μl per droplet). After that, the final product was collected by centrifugation at 12 000 rpm, washed twice with DI water. This protocol was also used for preparation of Ag@Pt, and Ag@Pd core–shell nanoplates by replacing the Au-precursor solution with potassium tetrachloroplatinate(II) (K_2PtCl_4, 0.1 M) and sodium tetrachloropalladate(II) (Na_2PdCl_4, 0.1 M) solutions respectively.

Preparation of Ag@PtPd trimetallic core–shell nanoplates

Trimetallic Ag@PtPd core–shell nanoplates were prepared by the same procedure as in the case of bimetallic core–shell nanostructures described above, except that we have used the seed-mediated co-reduction technique. Briefly, 0.1 ml of K_2PtCl_4 (0.1 M) solution and 0.1 ml of Na_2PdCl_4 (0.1 M) solution were co-dissolved and used to conformally deposit on the Ag nanoplates with all other conditions unaltered.

Aqueous-phase SERS measurement of CV adsorbed nanoplates

As-prepared Ag nanoplates, and AgM (Au, Pd, and Pt) core–shell and hollow nanoframes of the same concentration and volume were incubated with an aqueous solution containing 10 μl of crystal violet (CV, 1×10^{-6} M) for two hours. Then the solutions were transferred to a glass capillary for collecting the Raman spectra. The SERS spectra were collected using He–Ne laser with excitation wavelength of $\lambda_{ex} = 785$ nm. For all spectra, we used a laser power (P_{laser}) of 100 mW and a signal acquisition time of 8 s.

Materials characterization

The morphology of the as-prepared nanostructures was analyzed in a JEOL JEM-1010 transmission electron microscope (TEM) operating at 80 kV. The TEM images were obtained by drop casting the nanostructure dispersions on carbon coated

Cu-grids and drying at room temperature. Elemental distribution in the nanostructures was obtained through energy dispersive X-ray spectroscopy (EDX)-mapping in a Hitachi SU 8020 scanning transmission electron microscope (STEM). The XRD spectra were collected using an X-ray diffractometer (Rigaku Ultima IV, using Cu-Kα radiation) with parallel-beam geometry between 15 to 80° range. UV-visible (UV-vis) absorbance spectra were recorded using an Agilent 8453 UV-vis spectrophotometer with plastic cuvettes of 1 cm path length at room temperature in the range of 300–1100 nm. Raman spectra were collected on a Bruker (SENTERRA) Raman spectrometer equipped with a excitation light source of 785 nm He : Ne laser.

Results and discussion

Synthesis and structural characterization of Ag@Au core–shell nanoplates

Scheme 1 shows the steps involved in the formation of Ag-based core–shell and hollow nanostructures. We first explored preparation of the triangular Ag@Au core-shall nanoplates. In a typical synthesis, Ag nanoplates (edge length of 20–30 nm) were employed as the template for the controlled deposition of Au (Fig. S1†). In the subsequent deposition of Au on the Ag nanoplates, the Au precursor ($HAuCl_4$) was reduced with L-ascorbic acid (AA) in the presence of polyvinylpyrrolidone (PVP) at pH = 11. The TEM images reveal a triangular Ag@Au core–shell morphology, in which the triangular Ag seed template shape is preserved (Fig. 1a and b). Moreover, the scanning transmission electron microscopy (STEM) analysis unambiguously confirms the *Z*-contrast between the Ag core and Au shell (Fig. 1c). Additionally, compositional analysis by energy-dispersive X-ray spectroscopy (EDX)-elemental mapping, shown in Fig. 1d–f, indicates the presence of Ag elements in the core (red) while Au elements are located around the Ag nanoplate template (green) confirming the Ag@Au core–shell

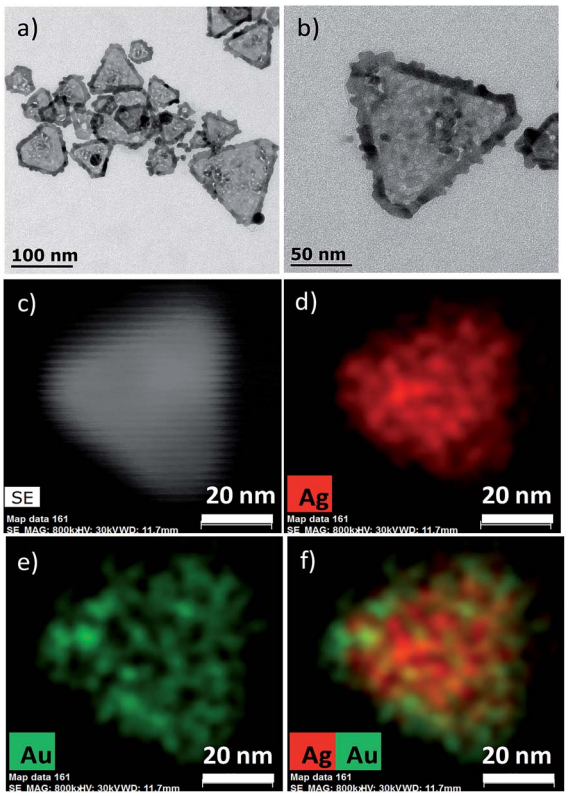

Fig. 1 (a) Low (b) high-magnification TEM images of the Ag@Au core–shell nanoplates. (c) STEM image of an individual Ag@Au nanoplate. (d–f) EDX-elemental mapping of a single Ag@Au nanoplate showing (d) Ag (red), (e) Au (green) and (f) overlapped Ag and Au elements (red and green), respectively.

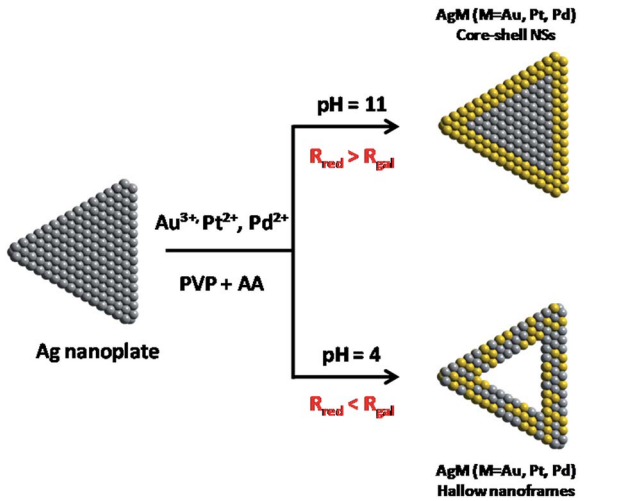

Scheme 1 Schematic illustration showing the synthetic steps for the preparation of AgM (Au, Pt, and Pd) triangular core–shell nanostructures and hollow nanoframes.

morphology. In addition, X-ray diffraction (XRD) result further verified the face centered cubic (fcc) structure of obtained Ag@Au core–shell nanoplates (Fig. S2†).

We hypothesize that the mechanism of Au deposition on the Ag nanoplates relies on the slow controlled addition of $HAuCl_4$, wherein the reduced Au atoms are initially deposited at the edges of the triangular Ag nanoplates *i.e.* the reaction occurs at the surface atoms with the lowest metal coordination number such as the tips of the Ag nanoplates, rather than the other faces.[3,35] The relative surface energies of the different facets in the Ag nanoplates are in the order of $\gamma_{111} < \gamma_{100} < \gamma_{110}$.[36] Therefore, the reduced Au adatoms preferentially start to nucleate and grow at the high-energy {110} facets *i.e.* on the edges of the Ag nanoplates.[36] The initially deposited Au atoms at the edges provide chemical stability and resist the etching events by oxidative dissolution at the edges and therefore the triangular shape would be maintained.[36,37] The deposited Au atoms at the edges could then diffuse into the other faces of the Ag nanoplates in a self-limiting fashion, thereby forming uniform Ag@Au core–shell nanoplates with uniform Au-shell thickness around the Ag nanoplates.[15,38] Thus, uniform deposition largely relies on the reduction rate. These results clearly indicate a seeded growth, in which the Au^{3+} is reduced rapidly with subsequent conformal deposition on the Ag nanoplates. The relatively higher reduction potential of $AuCl_4/Au$ (+1.498 *vs.*

SHE, standard hydrogen electrode) compared to that of Ag^+/Ag (0.779 V *vs.* SHE)[15,16] means that the oxidation of Ag is quite fast by Au^{3+}. Therefore, a strong reducing agent is essential to control the galvanic exchange between Ag and Au^{3+} and to accomplish uniform deposition of Au onto the Ag template. Previous reports have shown that the reduction power of the reducing agents (such as AA and glycine) can be boosted by increasing the pH of the reaction.[39] The slow addition of Au precursor solution at a relatively higher pH (pH = 11) significantly raises the reduction power of the AA, thus enabling faster reduction of Au atoms and subsequent formation of more active growth sites at the edges of Ag nanoplates. Under this condition, the reduction rate is greater than the galvanic replacement rate ($R_{red} > R_{gal}$), and the galvanic reaction can be suppressed, thus allowing uniform deposition of Au (Scheme 1).

In addition to the reduction rate, the surfactant PVP can also affect the final structure of Ag@Au core–shell nanoplates.[40–42] Specifically, PVP can significantly block the oxidative etching events and it preferentially binds with the reduced Au atoms to achieve homogeneous core–shell nanostructure by preserving the original triangular Ag seed nanoplate shape.[40] Additionally, PVP could serve as a mild reducing agent due to the presence of hydroxyl (–OH) side groups, which is negligible compared with the high reducing power of AA in the current synthesis.[43] To unravel the role of PVP in the synthesis, we have performed two control experiments without introducing PVP and higher PVP content with otherwise identical conditions. The TEM image of Ag@Au nanoplates obtained without introduction of PVP (Fig. S3†), reveals the formation of significant amount of agglomerated small AuNPs attached to the surface of the Ag nanoplates. In contrast, the higher PVP content (twice the amount of PVP used in the standard procedure) yielded porous Ag@Au nanostructures with a slightly different shape (Fig. S4†). These results suggest the equilibration of ratio of PVP and Ag nanoplate seeds by introducing the exact amount of PVP into the synthesis, which proves to be crucial for achieving the homogeneous Au-shell on the Ag nanoplate template. In addition, we also replaced PVP with another stabilizing agent CTAB, which has been widely considered for the colloidal synthesis of nanocrystals.[3,44] The resultant products were uniform hexagonal shaped Ag@Au core–shell nanoparticles (Fig. S5†). This effect is due to the selective adsorption of CTAB on the (100) a facet of Ag nanoplates and the occurrence of oxidative dissolution selectively at the edges of the Ag nanoplate seeds during the addition of Au^{3+} aqueous precursor salt.[35] It is evident that the selection of a stabilizing agent is also necessary for the formation of Ag@Au nanoplates.

Synthesis of bimetallic/multimetallic AgM (M = Pt and Pd) core–shell nanoplates

To demonstrate the versatility of our approach, we synthesized other bimetallic combinations: Ag@Pt and Ag@Pd core–shell nanoplates systems. The synthesis was carried out under similar reaction conditions described above for the Ag@Au core–shell nanoplates by only replacing the Au precursor with Pt and Pd precursor solutions, respectively (see experimental details). Fig. 2a and d show the TEM and EDX-elemental mapping results for the Ag@Pt system; in spite of a slight difference in the deposition uniformity, the formation of core–shell morphology is evident. Similarly, uniform deposition is also observed in the case of Ag@Pd (Fig. 2b and e). The slight non-uniform deposition in the case of Ag@Pt nanoplates may be the consequence of higher lattice mismatch between Ag and Pt compared to Ag and Pd elements.

This method can be extended to the preparation of multimetallic Ag@PtPd nanoplates with Pt and Pd precursors ($PtCl_6$ and H_2PdCl_4) at a 2 : 1 molar ratio simultaneously co-reduced with all other conditions unaltered. Interestingly, the final product is slightly changed from triangular shape into a heart-like shape with porous features and a silver core with PtPd alloy preferentially on the shell (Fig. 2c and f). This scenario arises due to the higher reduction potential of Ag compared to Pt and Pd; the standard reduction potential of (Ag/Ag^+), ($PtCl_6^{2-}/Pt$), and ($PdCl_4^{2-}/Pd$) are +0.8, +0.591 and +0.68 V *vs.* SHE, respectively. These results are consistent with reports by Kang *et al.* for the deposition of PdPt on Au octahedral NCs to form Au@PdPt core–shell NPs, in which the dendritic-like PdPt shell was formed on the Au octahedral core when reduced simultaneously with both AA and hydrazine.[45] In general, due to the differences in the reduction potential, large lattice mismatch and high intrinsic surface free energy of Pt/Pd, the deposition of Pt/Pd or PtPd co-reduced on the Ag seed is dominated by the island growth mode (Volmer–Weber mode), resulting in the formation of different shapes.[46] Notably, similar to the Ag@Au nanoplates, the reduced PtPd atoms are initially deposited on the corner sites of the triangular Ag seeds and then the deposited PtPd atoms diffuse from the edges to the side faces of the Ag nanoplates. The morphology of the final products largely relies on the difference in the deposition rate of PtPd atoms (R_{dep}) and rate of surface diffusion (R_{dif}).[27,33,47] The heart-like shapes were formed at pH = 11 due to the deposition of PtPd atoms being higher than the surface diffusion (*i.e.* $R_{dep} > R_{dif}$). Therefore, due to inadequate surface diffusion, the deposited PtPd atoms partially diffuse to other faces while most of them reside on the edges of the triangular Ag nanoplates, resulting in the formation of heart-like Ag@PtPd core–shell nanostructures.

The UV-vis spectroscopy was used to study the optical properties of the as-prepared core–shell nanoplates. Fig. 3 shows the UV-vis spectra of all the core–shell nanoplates. The LSPR peak of the Ag@Au core–shell nanoparticles is largely shifted near the NIR region (780 nm), compared to the other three cases. This large shift is due to the large variation in the collective oscillations of the surface free electrons after Au-shell formation.[48] There are no significant SPR peak shifts in the case of Ag@Pt, Ag@Pt, and Ag@PtPd core–shell nanoplates which is mainly due the damping effect caused by the imaginary part of Pt/Pd dielectric function.[49,50]

The pH of the reaction system is the key to controlling the galvanic replacement and selective formation of core–shell nanoplates. To clearly elucidate this effect, we performed further control experiments at a relatively low pH (pH = 4) by adding a certain amount of 0.2 M of HCl, that resulted in well-defined bimetallic AgM (Au, Pd, and Pt) hollow nanoframes

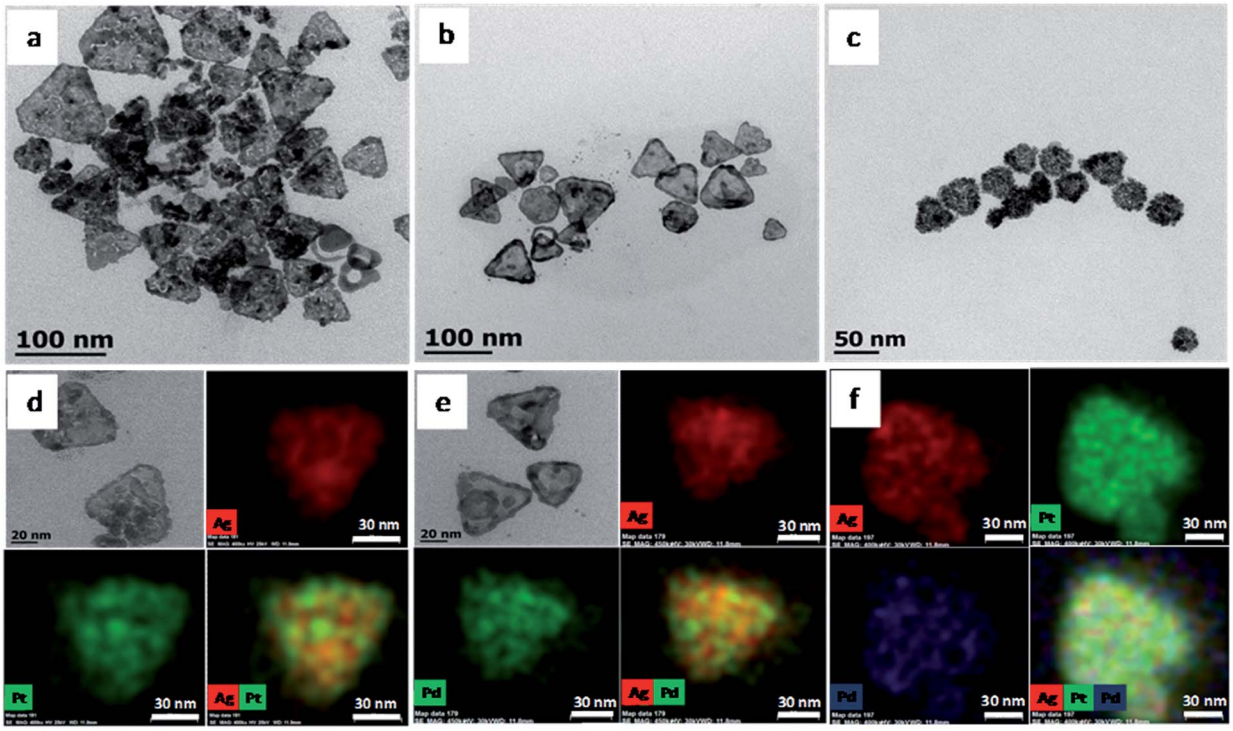

Fig. 2 TEM and STEM-EDX mapping images for (a and d) Ag@Pt, (b and e) Ag@Pd, and (c and f) Ag@PdPt nanoplates, respectively, prepared using the same procure, except for the different metal precursors.

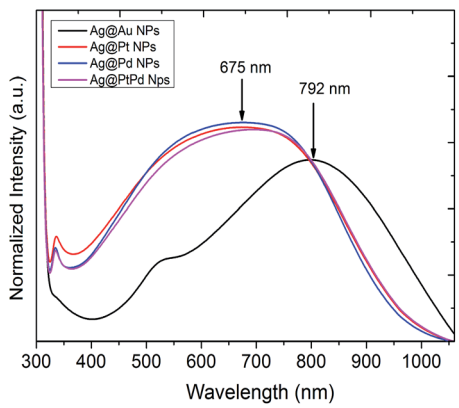

Fig. 3 UV-vis spectra of the Ag@Au, Ag@Pt, Ag@Pd, and Ag@PtPd core–shell nanoplates.

(Fig. 4). Moreover, Ag@PtPd can also form trimetallic triangular hollow nanostructure (Fig. S6†). These are driven by the galvanic replacement reaction at relatively low pH. During this stage, the galvanic reaction is dominant (*i.e.* $R_{gal} > R_{red}$), thereby leading to the formation of hollow nanostructures with controllable interior pore and composition (Scheme 1). A similar phenomenon was reported recently for Ag@Pt nanocage,[27] Ag@PdAg nanocubes,[14] Ag@AuPd nanocubes,[24] and Au@AuPt nanoframes.[51] These studies have found that the reduction power of AA is suppressed at pH = 4 and the galvanic replacement reaction is dominant. In addition, the use of HCl in the reaction released Ag ions by galvanic reaction rapidly precipitating as AgCl, which grew on the triangular Ag seeds and served as secondary template for co-deposition of Au, Pt, and Pd on the Ag seeds, respectively.

SERS analysis

In comparison with the usual spherical nanocrystals, anisotropic bimetallic nanostructures exhibit largely enhanced SERS activity because of the presence of sharp tips, which can serve as active "hot spots" for enhancing the SERS signal.[31,52,53] Therefore, we have carried out the SERS analysis of the as-prepared core–shell and hollow nanostructures. The SERS performance was measured in aqueous solution containing a fixed concentration of NPs absorbed with crystal violet (CV, 10^{-6} M) as probe molecule since CV binds naturally to the NP surface without further chemical modifications. Fig. 5a and b compares the SERS spectra of CV absorbed on all the nanoplates and hollow nanoframes with a laser excitation wavelength of 785 nm. Fig. 5a shows several prominent peaks at 206, 422, 726, 803, 910, 1173, 1389, 1589, 1620 cm^{-1}, corresponding to the characteristic peak positions of CV molecules.[54] The Ag@Au core–shell nanostructures exhibit well-defined SERS signal compared to Ag@Pt, Ag@Pd and Ag@PdPt nanostructures.

The enhancement factors (EFs) were estimated according to the following expression,

$$EF = \frac{I_{SERS}}{N_{SERS}} \frac{I_{Nor}}{N_{Nor}} \quad (1)$$

where, I_{SERS} and I_{Nor} are the signal intensities of SERS and normal Raman spectra of CV at the same band (here, ~1620

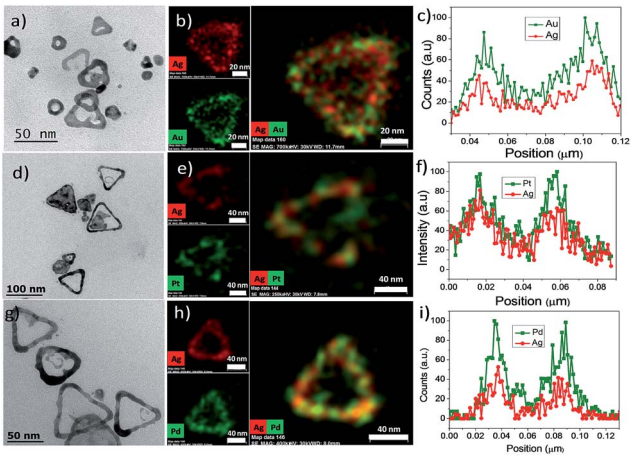

Fig. 4 TEM images (left) and EDX-elemental maps with EDX-line profile (right) of bimetallic nanoframes for (a–c) Ag@Au, (d–f) Ag@Pt, and (g–i) Ag@Pd, respectively. pH here was maintained at 4.

cm^{-1}), and N_{SERS} and N_{Nor} represent the corresponding number of molecules in the focused incident laser spot. Presuming that the CV molecules were evenly distributed in the aqueous solution, N_{SERS} and N_{Nor} were substituted with the concentration of CV (*i.e.* 1.0×10^{-6} M and 1.0×10^{-3} M, respectively). Based on the intensity of the peak located at 1620 cm^{-1}, the estimated SERS enhancement factors for AgM (Au, Pt, Pd) core–shell nanoplates and hollow nanostructures are displayed in Fig. 5c and d. Compared with Ag@Pt and Ag@Pd nanostructures and hollow nanoframes, the Ag@Au core–shell nanoplates show higher EFs of *ca.* 4.73×10^3. This value is approximately two orders magnitude higher than for spherical nanoparticles.[52]

We ascribe the significantly higher SERS efficiency of Ag@Au core–shell nanoplates to the effective coupling of LSPR peaks with the laser excitation wavelength 785 nm used to obtain the Raman spectra.[55,56] Nevertheless, weaker SERS EFs of Ag@Pt, Ag@Pd, and Ag@PtPd nanostructures are perhaps due to weak coupling between their free electrons to the excitation wavelength as confirmed from the UV-vis results (Fig. 3). Our results are consistent with previous reports on the SERS EF value of Pd nanocubes being very low compared to the Ag nanocubes.[57,58] The chemical adsorption of analyte molecules on the nanoparticle surface significantly affect the SERS response. The strong adsorption ability of CV molecules onto the Au surfaces could further contribute to the improvement in the SERS response for the Ag@Au core–shell nanoplates.[14]

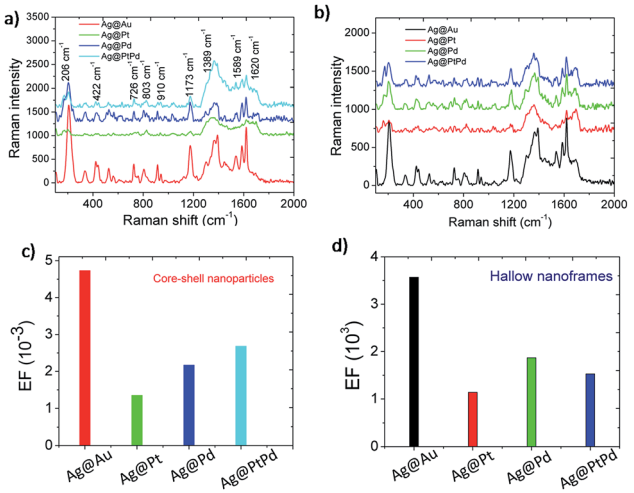

Fig. 5 Raman spectra of AgM (Au, Pt, and Pd) core–shell and hollow nanostructures.

Conclusions

We have successfully demonstrated a general strategy for the pH-dependent controlled synthesis of AgM (Au, Pt and Pd) bimetallic/multimetallic core–shell and hollow nanostructures. Our results reveal that the pH of the reaction is the leading factor directly influencing the galvanic reaction and the resulting products. By increasing the pH (pH = 11), the reduction rate is dominated by the AA, leading to the formation of uniform core–shell nanostructures, whereas the galvanic replacement rate dominates at relatively low pH yielding well-defined hollow nanoframes. Significantly, the Ag@Au core–shell nanoplates show much enhanced SERS performance compared to Ag@Pt, Ag@Pd and Ag@PtPd core–shell nanoplates. Thus, the present approach provides unique possibilities for creating rationally designed nanoscale materials with desired architectures for the promising applications in SERS-based monitoring of catalytic reactions, plasmonics and sensing.

Acknowledgements

This work was supported by the DGAPA-UNAM post-doctoral fellowship. The authors would like to acknowledge PAPIIT-DGAPA for financial support with grant No. IN113317. Also, Dra. Genoveva Hernandez for the SERS measurements and Ma. Lourdes Palma Tirado (Campus UNAM Juriquilla, Qro) for TEM measurements.

Notes and references

1 S. Liu, H. Tao, L. Zeng, Q. Liu, Z. Xu, Q. Liu and J.-L. Luo, *J. Am. Chem. Soc.*, 2017, **139**, 2160–2163.
2 B. Jiang, C. Li, V. Malgras, M. Imura, S. Tominaka and Y. Yamauchi, *Chem. Sci.*, 2016, **7**, 1575–1581.
3 M. N. O'Brien, M. R. Jones, K. L. Kohlstedt, G. C. Schatz and C. A. Mirkin, *Nano Lett.*, 2015, **15**, 1012–1017.
4 H. Yockell-Lelièvre, F. Lussier and J. F. Masson, *J. Phys. Chem. C*, 2015, **119**, 28577–28585.
5 Z. Matharu, P. Daggumati, L. Wang, T. S. Dorofeeva, Z. Li and E. Seker, *ACS Appl. Mater. Interfaces*, 2017, **9**, 12959–12966.
6 X. Yang, M. Yang, B. Pang, M. Vara and Y. Xia, *Chem. Rev.*, 2015, **115**, 10410–10488.
7 I. Pastoriza-santos, L. M. Liz-marzán, D. G. Shchukin, I. Pastoriza-santos and L. M. Liz-marza, *J. Mater. Chem.*, 2008, **18**, 1724–1737.
8 H. Hou, P. Wang, J. Zhang, C. Li and Y. Jin, *ACS Appl. Mater. Interfaces*, 2015, **7**, 18038–18045.

9 D. E. Charles, D. Aherne, M. Gara, D. M. Ledwith, Y. K. Gun, J. M. Kelly, W. J. Blau and M. E. Brennan-fournet, *ACS Nano*, 2010, **4**, 55–64.
10 Q. Zhang, Y. Hu, S. Guo, J. Goebl and Y. Yin, *Nano Lett.*, 2010, **10**, 5037–5042.
11 B. Loganathan, V. L. Chandraboss, S. Senthilvelan and B. Karthikeyan, *Phys. Chem. Chem. Phys.*, 2015, **17**, 21268–21277.
12 R. G. Chaudhuri and S. Paria, *Chem. Rev.*, 2012, **112**, 2373–2433.
13 K. D. Gilroy, A. Ruditskiy, H. Peng, D. Qin and Y. Xia, *Chem. Rev.*, 2016, **116**, 10414–10472.
14 J. Li, J. Liu, Y. Yang and D. Qin, *J. Am. Chem. Soc.*, 2015, **137**, 7039–7042.
15 M. M. Shahjamali, M. Bosman, S. Cao, X. Huang, S. Saadat, E. Martinsson, D. Aili, Y. Y. Tay, B. Liedberg, S. C. J. Loo, H. Zhang, F. Boey and C. Xue, *Adv. Funct. Mater.*, 2012, **22**, 849–854.
16 L. Xu, Z. Luo, Z. Fan, X. Zhang, C. Tan, H. Li, H. Zhang and C. Xue, *Nanoscale*, 2014, **6**, 11738–11743.
17 H. Liu, T. Liu, L. Zhang, L. Han, C. Gao and Y. Yin, *Adv. Funct. Mater.*, 2015, **25**, 5435–5443.
18 M. Sun, H. Qian, J. Liu, Y. Li, S. Pang, M. Xu and J. Zhang, *RSC Adv.*, 2017, **7**, 7073–7078.
19 C. Xue, J. E. Millstone, S. Li and C. A. Mirkin, *Angew. Chem., Int. Ed.*, 2007, **46**, 8436–8439.
20 J. Zhang, Y. Tang, K. Lee and M. Ouyang, *Science*, 2010, **327**, 1634–1638.
21 T. Bian, H. Zhang, Y. Jiang, C. Jin, J. Wu, H. Yang and D. Yang, *Nano Lett.*, 2015, **15**, 7808–7815.
22 S.-C. Hsu, Y.-C. Chuang, B. T. Sneed, D. A. Cullen, T.-W. Chiu and C.-H. Kuo, *Nano Lett.*, 2016, **16**, 5514–5520.
23 Y. Xia, K. D. Gilroy, H.-C. Peng and X. Xia, *Angew. Chem., Int. Ed.*, 2016, **55**, 2–38.
24 H. Ataee-Esfahani, M. Imura and Y. Yamauchi, *Angew. Chem., Int. Ed.*, 2013, **52**, 13611–13615.
25 V. Malgras, H. Ataee-Esfahani, H. Wang, B. Jiang, C. Li, K. C. W. Wu, J. H. Kim and Y. Yamauchi, *Adv. Mater.*, 2016, **28**, 993–1010.
26 B. Jiang, C. Li, J. Tang, T. Takei, J. H. Kim, Y. Ide, J. Henzie, S. Tominaka and Y. Yamauchi, *Angew. Chem., Int. Ed.*, 2016, **55**, 10037–10041.
27 X. Yang, L. T. Roling, M. Vara, A. O. Elnabawy, M. Zhao, Z. D. Hood, S. Bao, M. Mavrikakis and Y. Xia, *Nano Lett.*, 2016, **6**, 6644–6649.
28 G. S. Metraux, Y. C. Cao, R. Jin and C. A. Mirkin, *Nano. Lett.*, 2003, **3**, 519–522.
29 C. Gao, Z. Lu, Y. Liu, Q. Zhang, M. Chi, Q. Cheng and Y. Yin, *Angew. Chem., Int. Ed.*, 2012, **51**, 5629–5633.
30 Y. Yang, J. Liu, Z. Fu and D. Qin, *J. Am. Chem. Soc.*, 2014, **136**, 8153–8156.
31 J. Zhang, S. A. Winget, Y. Wu, D. Su, X. Sun, Z. X. Xie and D. Qin, *ACS Nano*, 2016, **10**, 2607–2616.
32 M. Yang, Z. D. Hood, X. Yang, M. Chi and Y. Xia, *Chem. Commun.*, 2017, **53**, 1965–1968.
33 X. Xia, S. Xie, M. Liu, H.-C. Peng, N. Lu, J. Wang, M. J. Kim and Y. Xia, *Proc. Natl. Acad. Sci. U. S. A.*, 2013, **110**, 6669–6673.
34 Y. Xia, J. Ye, K. Tan, J. Wang and G. Yang, *Anal. Chem.*, 2013, **85**, 6241–6247.
35 M. N. O. Brien, M. R. Jones, K. A. Brown and C. A. Mirkin, *J. Am. Chem. Soc.*, 2014, **136**, 7603–7606.
36 M. M. Shahjamali, M. Salvador, M. Bosman, D. S. Ginger and C. Xue, *J. Phys. Chem. C*, 2014, **118**, 12459–12468.
37 D. Aherne, D. E. Charles, M. E. Brennan-Fournet, J. M. Kelly and Y. K. Gunko, *Langmuir*, 2009, **25**, 10165–10173.
38 S. Xie, S. Choi, N. Lu, L. Roling, J. A. Herron, L. Zhang, J. Wang, M. J. Kim, Z. Xie, M. Mavrikakis and Y. Xia, *Nano Lett.*, 2014, **14**, 3570–3576.
39 S. Liang, X. Liu, Y. Yang and Y. Wang, *Nano Lett.*, 2012, **12**, 5281–5286.
40 H. Sun, J. He, J. Wang, S. Y. Zhang, C. Liu, T. Sritharan, S. Mhaisalkar, M. Y. Han, D. Wang and H. Chen, *J. Am. Chem. Soc.*, 2013, **135**, 9099–9110.
41 W. A. Al-Saido, H. Feng and K. A. Fichthorn, *Nano Lett.*, 2012, **12**, 997–1001.
42 N. Murshid and V. Kitaev, *Chem. Commun.*, 2014, **50**, 1247–1249.
43 Y. Yin and A. P. Alivisatos, *Nature*, 2005, **437**, 664–670.
44 D. K. Smith and B. A. Korgel, *Langmuir*, 2008, **24**, 644–649.
45 S. W. Kang, Y. W. Lee, Y. Park, B. Choi, J. W. Hong and K. Park, *ACS Nano*, 2013, **7**, 7945–7955.
46 M. Meng, Z. Fang, C. Zhang, H. Su, R. He, R. Zhang, H. Li, Z.-Y. Li, X. Wu, C. Ma and J. Zeng, *Nano Lett.*, 2016, **16**, 3036–3041.
47 S. Xie, S. Choi, N. Lu, L. Roling, J. A. Herron, L. Zhang, J. Wang, M. J. Kim, Z. Xie, M. Mavrikakis and Y. Xia, *Nano Lett.*, 2014, **14**, 3570–3576.
48 X. Wang, Z. Zhang and G. V Hartland, *J. Phys. Chem. B*, 2005, **109**, 20324–20330.
49 P. Mohan, M. Takahashi, K. Higashimine, D. Mott and S. Maenosono, *Langmuir*, 2017, **33**, 1687–1694.
50 H. Zhang, Z. Liu, X. Kang, J. Guo, W. Ma and S. Cheng, *Nanoscale*, 2016, **8**, 2242–2248.
51 S. Han, G. Zhou, Y. Fu, Y. Ma, L. Xu, C. Zou, W. Chen, Y. Yang and S. Huang, *Nanoscale*, 2015, **7**, 20414–20425.
52 K. L. Kelly, E. Coronado, L. L. Zhao and G. C. Schatz, *J. Phys. Chem. B*, 2003, **107**, 668–677.
53 X. Wei, Q. Fan, H. Liu, Y. Bai, L. Zhang, H. Zheng, Y. Yin and C. Gao, *Nanoscale*, 2016, **8**, 15689–15695.
54 M. N. Sanz-Ortiz, K. Sentosun, S. Bals and L. M. Liz-Marzán, *ACS Nano*, 2015, **9**, 10489–10497.
55 S. K. Cha, J. H. Mun, T. Chang, S. Y. Kim, J. Y. Kim, H. M. Jin, J. Y. Lee, J. Shin, K. H. Kim and S. O. Kim, *ACS Nano*, 2015, **9**, 5536–5543.
56 M. Li, J. W. Kang, R. R. Dasari and I. Barman, *Angew. Chem., Int. Ed.*, 2014, **53**, 14115–14119.
57 J. M. Mclellan, Y. Xiong, M. Hu and Y. Xia, *Chem. Phys. Lett.*, 2006, **417**, 230–234.
58 Y. Zhang, X. Gao and M. J. Weaver, *J. Phys. Chem.*, 1993, **97**, 8656–8663.

